Earth-Science Reviews 147 (2015) 54–64

Contents lists available at ScienceDirect

Earth-Science Reviews

journal homepage: www.elsevier.com/locate/earscirev

GNSS ionospheric seismology: Recent observation evidences and characteristics

Shuanggen Jin [a,b,*], Giovanni Occhipinti [c], Rui Jin [a,d]

[a] Shanghai Astronomical Observatory, Chinese Academy of Sciences, Shanghai 200030, China
[b] Department of Geomatics Engineering, Bulent Ecevit University, Zonguldak 67100, Turkey
[c] Institut de Physique du Globe de Paris, Paris 94107, France
[d] University of Chinese Academy of Sciences, Beijing 100049, China

ARTICLE INFO

Article history:
Received 5 November 2014
Accepted 4 May 2015
Available online 11 May 2015

Keywords:
Ionospheric seismology
Ionospheric disturbance
GNSS
TEC

ABSTRACT

The detail and nature of earthquakes are still challenging from traditional technique observations, e.g., seismometers and strong motion accelerographs. Nowadays, the ionospheric total electron content (TEC) can be obtained from ground-based global navigation satellite systems (GNSS) and space-borne GNSS Radio Occultation, which can be used to investigate the seismo-ionospheric disturbances and may provide insights on the earthquake. In this paper, GNSS ionospheric seismology is presented and reviewed, including methods, observation results and characteristics. Case studies of the 2008 Wenchuan earthquake and 2011 Japan earthquake are presented using ground-based GNSS observations. Significant co-/post-seismic ionospheric anomalies are found from continuous GNSS observations near the epicenters, showing that the seismic ionospheric total electron content (TEC) disturbances were derived mainly from the main shock. The detailed pattern and evolution of the ionospheric disturbance are revealed by denser GNSS observations. Some simulations explore the nature of the ionospheric perturbation, highlighting that acoustic-gravity waves are generated close to the epicenter, and that surface Rayleigh waves and tsunamis generate in the atmosphere/ionosphere acoustic and gravity waves respectively. These waves are induced by solid-Earth/ocean and atmosphere coupling at the ground or ocean interface with the atmosphere propagating upward until the ionosphere create strong perturbation in plasma density and plasma velocity.

Contents

1. Introduction

1.1. History and status

Earthquakes often occur and result in civilian casualties and huge damages. The earthquake is a very complex and broad topic, which is related to various scale motions of the Earth's surface mass and interior as well as the microscopic processes, such as the generation of electric charge and chemical reactions (Pulinets and Boyarchuk, 2004). Up to now, it is still difficult and challenging to understand the effects related to earthquakes comprehensively and profoundly (Jin et al., 2013). The recent worldwide earthquakes with large magnitudes are located in Sumatra (Mw = 9.1 in 2004, Mw = 8.9 in 2012), Wenchuan (Mw = 8.0 in 2008), Chile (Mw = 8.8 in 2010) and Tohoku (Mw = 9.0 in 2011).

---

* Corresponding author. Tel.: +86 21 34775292; fax: +86 64384618.
E-mail addresses: sgjin@shao.ac.cn, sg.jin@yahoo.com (S. Jin).

http://dx.doi.org/10.1016/j.earscirev.2015.05.003

Those events were associated to infrastructure damages and tragic loss of lives induced by the strong ground motion at the epicenter or by the tsunami in the far field (der Hilst, 2008). Monitoring and quick responses to earthquakes are still a major objective for many countries. The worldwide seismometers could estimate rapidly the location, the magnitude and the focal mechanism of earthquakes, but the detailed rupture and atmospheric/ionospheric response are still difficult to be understood deeply, due to the lack of dense near-field observations. The horizontal extent of the source plays a fundamental role in the risk assessment of earthquake and its secondary disasters, such as tsunami and landslide for warning system. Global navigation satellite systems (GNSS), Interferometric Synthetic Aperture (InSAR), strong motion measurements and gravity measurement could provide unique insights on the size and kinematic rupture of the earthquake (Jin et al., 2010; Cambiotti et al., 2011). However, the quick response to earthquakes is still difficult and challenging based on current traditional observations due mostly to the lack of near field observations.

GNSS is a powerful tool not only for the crust displacement but also the seismic ionospheric variation, especially for regions with dense GNSS continuous operating stations. GNSS provides us an opportunity to monitor the detail of fault rupture with high spatial–temporal resolution and moreover it gives us a new perspective to understand the earthquake effect with seismic ionospheric disturbance. The first ionospheric perturbation related to seismic events was detected in 1964, after the Alaska earthquake (M 9.2, March 28, 1964), mainly based on the analyses of Doppler records and vertical sounder ionograms (Davies and Baker, 1965; Leonard and Barnes, 1965). The acoustic-gravity wave associated to tectonic deformation following the earthquake was detectable at the F region (Row, 1966; Row, 1967). These preliminary results implicated that the energy released during the rupture of the fault was not only propagating in the solid Earth but also leaking out to the Earth atmosphere and even to the ionosphere. The vertical displacement, at teleseismic distance, induced by Rayleigh wave produces an acoustic wave that propagates vertically until the ionosphere by dynamic coupling. During the upward propagation, the double effects of the conservation of kinetic energy and the exponential decreasing of the atmospheric density, strongly amplify the acoustic wave that reaching the ionosphere creates strong variation in the plasma density (detected by GPS, see below) and plasma velocity (detected by Doppler sounder). Particular emphasis was related to the Doppler sounder detection of the ionospheric signature induced by Rayleigh wave propagation. Consequently, a new perspective of earthquake effects is provided by the characteristic analysis of seismic ionospheric disturbance estimated through observing the ionosphere (Najita and Yuen, 1979; Tanaka et al., 1984; Artru et al., 2004; Jin et al., 2010; Occhipinti et al., 2010).

Global navigation satellite systems (GNSS), including United States' GPS, European Union's GALILEO, Russia's GLONASS and China's BeiDou Navigation Satellite System (BDS) as well as a number of regional Space Based Augmentation Systems, have been widely used for positioning, navigation and timing (PNT) (Jin et al., 2010). In addition, when GNSS signals propagate through the Earth's atmosphere, the GNSS signals are delayed by the tropospheric and ionospheric refraction, resulting in lengthening of the geometric path of GNSS signals and the variation of signals' group velocity and phase velocity, namely so-called tropospheric and ionospheric delays. Nowadays, the tropospheric and ionospheric delays can be retrieved from ground-based GNSS networks and space-borne GNSS Radio Occultation (Schreiner et al., 1999; Wickert et al, 2001; Jin et al., 2004; Jin et al, 2008a; Afraimovich et al, 2011; Jakowski et al., 2011; Jin et al, 2011). Since the first time the total electron content (TEC) anomalous signal was observed by Calais and Minster (1995) after the Northridge earthquake in California on January 17, 1994, numerous studies have been intended to study pre/co-seismic ionospheric disturbances related to earthquakes (Liu et al., 2004; Afraimovich et al., 2010; Heki and Enomoto, 2013).

For instance, Ducic et al. (2003) detected TEC perturbations related to the acoustic waves associated with the Rayleigh waves measured by the dense Californian network following the Denali Earthquake. The measurement of the horizontal speed of the ionospheric perturbations roughly agrees with the speed of Rayleigh waves propagating on the Earth surface. Heki and Ping (2005) revealed the apparent velocity and directivity based on the traveling time diagram for the 2003 Tokachi-oki earthquake (Mw = 8.3) from GEONET GPS observations, and highlighted a north–south asymmetry of the seismic ionospheric effects related to the geomagnetic field inclination. Co-seismic ionospheric disturbances detected by GNSS data near the epicenter were thought to be related to the acoustic-gravity waves excited sequentially along the rupture of the fault (Heki et al., 2006). Recently a more comprehensive understanding of seismic ionospheric effects for the 2011 Tohoku earthquake (M 9.0) was revealed by abundant GNSS observations collected by GEONET near the epicenter (Liu et al., 2011; Rolland et al., 2011; Tsugawa et al., 2011; Occhipinti et al., 2013; Jin et al., 2014). The extremely dense TEC observation performed by the GEONET network clearly highlighted acoustic-gravity waves generated at the epicenter, acoustic waves coupled with Rayleigh wave, as well as gravity waves coupled with the propagation of the following tsunami (Occhipinti et al., 2013; Coisson et al., 2011). As clearly showed by Shinagawa et al. (2013) and Rolland et al. (2011), the TEC observations supplied by the dense GEONET network during the 11 March 2011 Tohoku earthquake and the 25 September 2003 Tokachi-Oki earthquake, provide a unique chance to investigate the seismic ionospheric disturbances related to the fault rupture in vicinity of the epicenter, as well as TEC perturbation related to the propagation of Rayleigh waves and tsunami in far-field. The Japanese GNSS network (GEONET) is denser with over 1200 continuous GNSS stations operated by Geographical Survey Institute (GSI) Japan. Astafyeva et al. (2013) showed the possibilities to estimate the parameters of seismic source by observing the first post-seismic signal appearing in the ionosphere 8 min after the rupture. As a result of the integrated nature of the TEC, the sensitivity of GPS measurement to the ionospheric perturbation related to the seismic activity is mainly limited to larger events. There are not enough earthquake events that are suitable for seismic ionospheric effect research, since most giant earthquake epicenters are always not located in regions with dense GNSS stations. Here the major events were recently investigated, e.g., 2002 Mw = 7.8 Denali earthquake (Ducic et al., 2003), 2003 Mw = 8.3 Tokachi-oki earthquake (Heki and Ping, 2005), 2004 Mw = 9.1 Sumatra earthquake (DasGupta et al., 2006; Heki et al., 2006; Liu et al., 2006; Occhipinti et al., 2006, 2013), 2006 Mw = 8.3 Kuril earthquake, the 2009 Mw = 8.1 Samoa earthquake and the 2010 Mw = 8.8 Chile earthquake (Rolland et al., 2010), the 2008 Mw = 8.0 Wenchuan earthquake (Jin et al., 2010), and the 2011 Mw = 9.0 Tohoku earthquake (Liu et al., 2011; Occhipinti et al., 2011; Tsugawa et al., 2011; Astafyeva et al., 2011). The seismic ionospheric disturbance amplitude and propagation characteristics are still not understood comprehensively following the earthquake with different magnitudes, focal mechanism and complex space weather. The mechanism of solid Earth/ocean–atmosphere–ionosphere coupling still needs to be improved for different cases and be verified with more GNSS measurements. Perevalova et al. (2014) examined the earthquakes with magnitudes from 4.1 to 8.8 in different regions (the Baikal region, Kuril Islands, Japan, Greece, Indonesia, China, New Zealand, Salvador, and Chile) and found a threshold magnitude of near Mw = 6.5, below which there were no pronounced earthquake-induced TEC disturbances (see Fig. 1). The seismic ionospheric disturbance amplitude increases proportionally with the earthquake magnitude generally. Comparing to strike-slip earthquake, normal/reverse fault earthquakes are usually followed with much more intense seismic ionospheric disturbances. It seems that the vertical displacement in the earthquake zone plays a more important role in the formation of seismic ionospheric disturbance. In addition, the geomagnetic condition also has a significant effect on the amplitude of seismic ionospheric disturbance. The

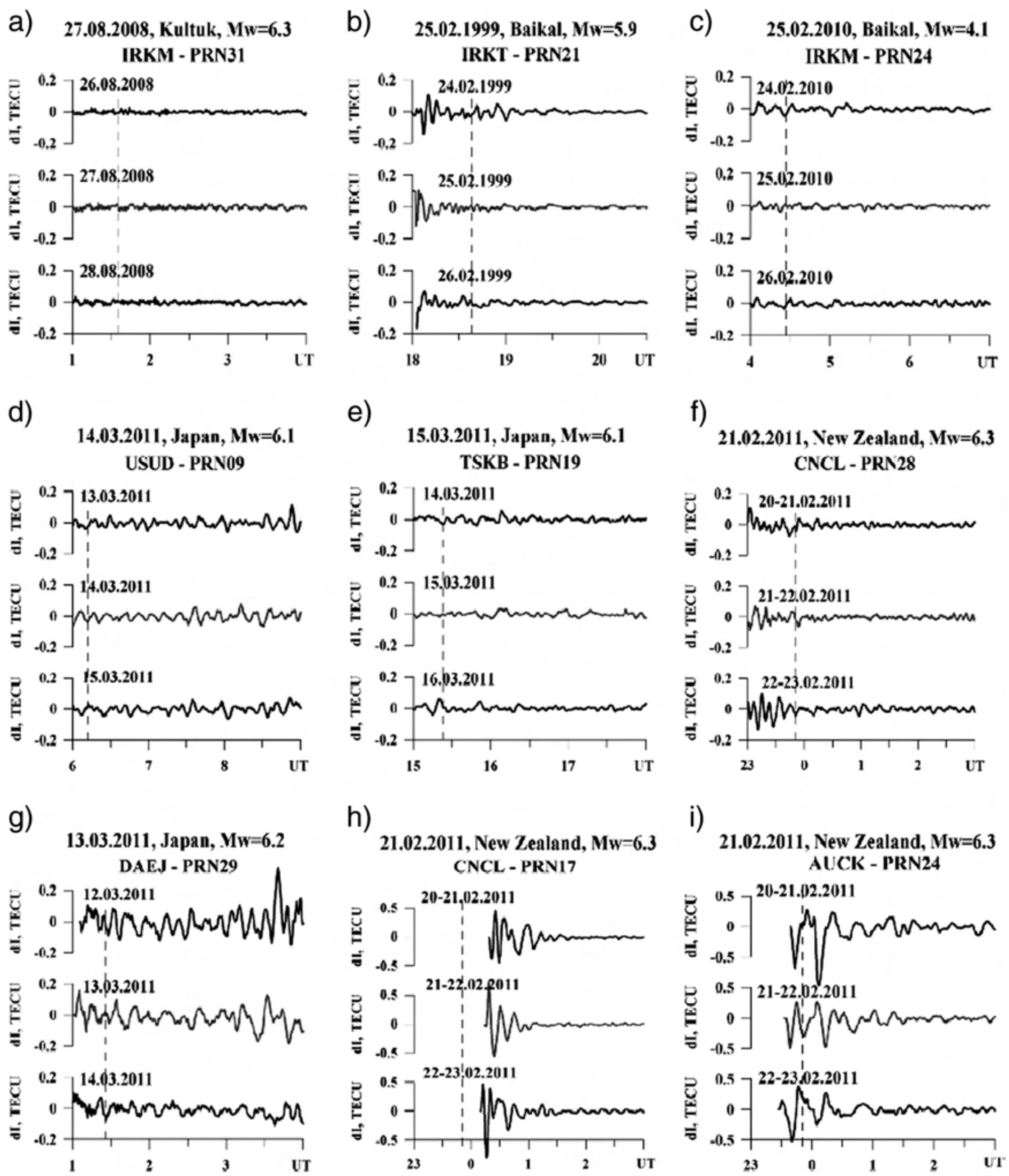

Fig. 1. TEC time series variations during Mw < 6.5 earthquakes occurred under quiet (a)–(f) and disturbed (g)–(i) conditions (Perevalova et al., 2014).

disturbance amplitude is higher relatively in disturbed geomagnetic days, which show that the filtered TEC time series are affected by not only earthquake generated disturbances but also the geomagnetic variations. As we have known, the variation of Earth's ionosphere is complex because of its high temporal dynamic and spatial discrepancy under the influence of various factors, such as space weather, natural event, and anthropogenic activities. It is still a challenge to extract clear and exact earthquake generated ionospheric disturbance for the worldwide earthquake occurred at different times with different external conditions (space weather, time of day, location, etc.). The relationship between the earthquake displacement and the ionospheric variation is not understood comprehensively up to now. The earthquake threshold and characteristics of seismic ionospheric disturbances following earthquakes with different magnitudes, focal mechanism, depth and external conditions are still a hot topic in next decades.

Furthermore, some controversial pre-seismic ionospheric anomalies were also observed in the TEC, NmF2 (F2 peak electron density) or HmF2 (F2 peak height) time series (Liu et al., 2006; Heki, 2011), however the mechanism is still unclear and the debate still existed. The pre-seismic ionospheric disturbances are found significantly because of the probability of a new earthquake precursor, while the lithosphere–atmosphere–ionosphere coupling (Pulinets and Ouzounov, 2011) is very complex. Ionospheric anomalies with several hours to several days before the main shock onset were widely reported (Liu et al, 2004; Heki and Enomoto, 2013). Kamogawa (2006) proposed the possible mechanisms for energy-transport from the lithosphere to the atmosphere–ionosphere in Fig. 2. Generally the atmospheric electric field generated on or near the ground surface during the seismic period is assumed to cause the ionospheric anomalies. However, whether these pre-seismic ionospheric disturbances are related to the earthquake

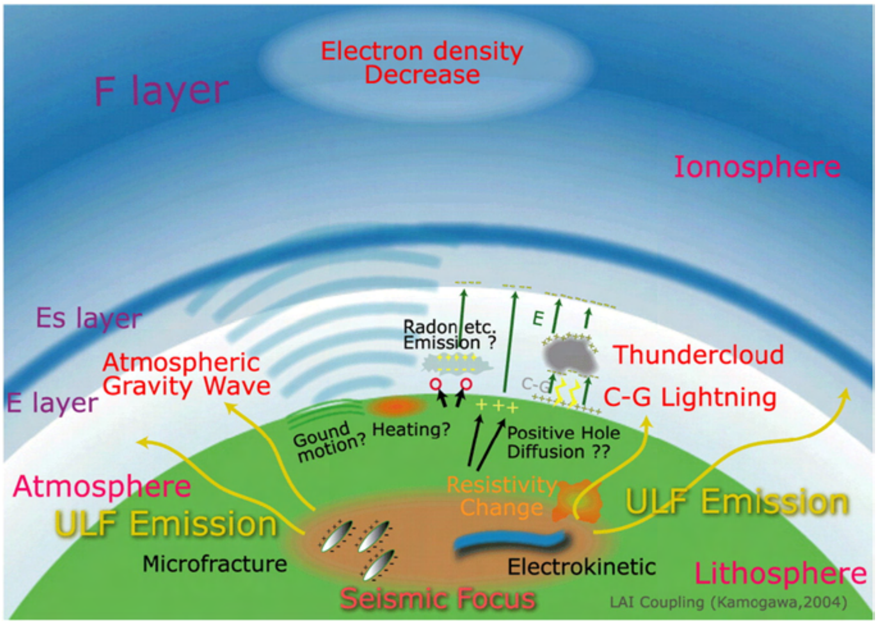

Fig. 2. Lithosphere–atmosphere–ionosphere coupling (Kamogawa, 2006).

or not is still controversial. It is difficult to extract the clear background variation of TEC. Up to now there is no explicit definition for pre-seismic ionospheric disturbances. One of the effects is the filtering or de-trended method, especially for considering the disturbance amplitude. Furthermore, the pre-seismic ionospheric anomaly is also interpreted as a fake signal induced by the data processing rather than the earthquake precursor (Kamogawa and Kakinami, 2013; Utada and Shimizu, 2014).

This work presents the GNSS ionospheric seismology, including methods, results, characteristics and coupling between solid-Earth and the fluid envelopes, nominally the ocean, the atmospheric and the ionosphere. Case studies are presented, including the 2008 Mw = 8.0 Wenchuan earthquake and the 2011 Mw = 9.0 Tohoku earthquake using the GPS data from the Crustal Movement Observation Network of China (CMONC) and the GPS Earth Observation Network of Japan (GEONET).

2. GNSS TEC observations and methods

The ionospheric delay is related to the frequency and dual-frequency GNSS receivers can estimate the ionospheric delay or total electron content (TEC) by measuring the modulations on the codes and carrier phases, e.g., GPS $f_1 = 1.57542$ GHz and $f_2 = 1.2276$ GHz. The equations of dual-frequency GNSS carrier phase (L) and code observations (P) are expressed as (Jin et al., 2008b; Wu et al., 2010):

$$\begin{aligned} L^i_{1,j} &= \rho^i_{0,j} - d^i_{ion,1,j} + d^i_{trop,j} + c\left(\tau^i - \tau_j\right) - \\ &\quad \lambda\left(b^i_{1,j} + N^i_{1,j}\right) + \varepsilon^i_{L,1,j} \\ L^i_{2,j} &= \rho^i_{0,j} - d^i_{ion,2,j} + d^i_{trop,j} + c\left(\tau^i - \tau_j\right) - \\ &\quad \lambda\left(b^i_{2,j} + N^i_{2,j}\right) + \varepsilon^i_{L,2,j} \end{aligned} \tag{1}$$

$$\begin{aligned} P^i_{1,j} &= \rho^i_{0,j} + d^i_{ion,1,j} + d^i_{trop,j} + c\left(\tau^i - \tau_j\right) + \\ &\quad d^i_1 + d_{1,j} + \varepsilon^i_{P,1,j} \\ P^i_{2,j} &= \rho^i_{0,j} + d^i_{ion,2,j} + d^i_{trop,j} + c\left(\tau^i - \tau_j\right) + \\ &\quad d^i_2 + d_{2,j} + \varepsilon^i_{P,2,j} \end{aligned} \tag{2}$$

where

L	is the carrier phase measurement,
P	is the code measurement,
ρ	is the true distance between the GNSS satellite and receiver,
d_{ion}	is the ionospheric delay,
d_{trop}	is the tropospheric delay,
c	is the speed of light in a vacuum,
τ	is the clock error of satellite and receiver,
b	is the phase advance of instrument bias,
d	is the code delay of instrument bias,
N	is ambiguity of the carrier phase, and
ε	is residuals in the GNSS measurement.

The ionopsheric delay can be obtained from the difference of dual-frequency GNSS phase and code observations. After combining the pseudorange and carrier phase observations of dual frequency GNSS, the slant TEC can be expressed as the following equation (Brunini and Azpilicueta, 2009; Jin et al., 2012):

$$\begin{aligned} STEC &= \frac{{f_1}^2{f_2}^2}{40.28\left({f_1}^2 - {f_2}^2\right)}\left(L_1 - L_2 + \lambda_1(N_1 + b_1) - \lambda_2(N_2 + b_2) + \varepsilon_L\right) \\ &= \frac{{f_1}^2{f_2}^2}{40.28\left({f_2}^2 - {f_1}^2\right)}\left(P_1 - P_2 - (d_1 - d_2) + \varepsilon_P\right) \end{aligned} \tag{3}$$

where $STEC$ is slant TEC, f is carrier phase frequency, L and P are carrier phase and pseudorange observations, respectively, λ is signal wavelength, N is the ambiguity, b and d are instrument biases for carrier phase and pseudorange, and ε is the sum of other items that are much smaller than the items described in Eq. (3), which could be ignored in our TEC analysis. For one continuous arc, the integer ambiguity and instrument bias can be considered as a constant. In order to get accurate STEC time series, the cycle slips should be detected and repaired, e.g., the TurboEdit (TE) algorithm (Blewitt, 1990), forward and backward moving window averaging (FBMWA) algorithm, a second-order and time-difference phase ionospheric residual (STPIR) algorithm (Cai et al., 2013). And then the STEC can be obtained using the clean GPS observations based on Eq. (3). Usually, it is assumed that all electrons in the ionosphere are concentrated in a thin shell called central ionospheric layer at 300–600 km altitude where the electron density is maximum. A cosine mapping function is used to convert STEC to vertical TEC (vTEC) (Schaer, 1999).

$$vTEC = STEC^{*}\cos\left(\arcsin\left(\frac{R\sin z}{R+H}\right)\right) \tag{4}$$

where R is the Earth radius, H is the thin shell height of the ionosphere and z is the satellite's zenith angle. The shell height is chosen by 300 km corresponding to the maximum electron density.

TEC series can be easily derived using Eqs. (1) and (2) with the clean GPS observations. Here the instrument bias is not considered, because it is constant in a short time that has no influence on TEC series variations after filtering. After obtaining TEC series, we use the filtering of 3–10 min window to remove the high frequency noise and TEC background trend caused by temporal and spatial variation at ionospheric pierce point (IPP). Here we set the window length as 3–10 min for mixed disturbances (including signal related with different modes), i.e. 1.7–5.6 mHZ, just covering the dominant frequencies of acoustic resonance modes between the ground surface and the lower thermosphere (Matsumura et al., 2011; Lognonné et al., 1998). Usually, Four-order zero-phase Butterworth filter is used because of its maximally flat magnitude. Moving average method could also be used to remove the background TEC variation (Tsugawa et al., 2011). Using TEC residual series, seismo-ionospheric anomalies can be detected during the earthquakes (Fig. 3).

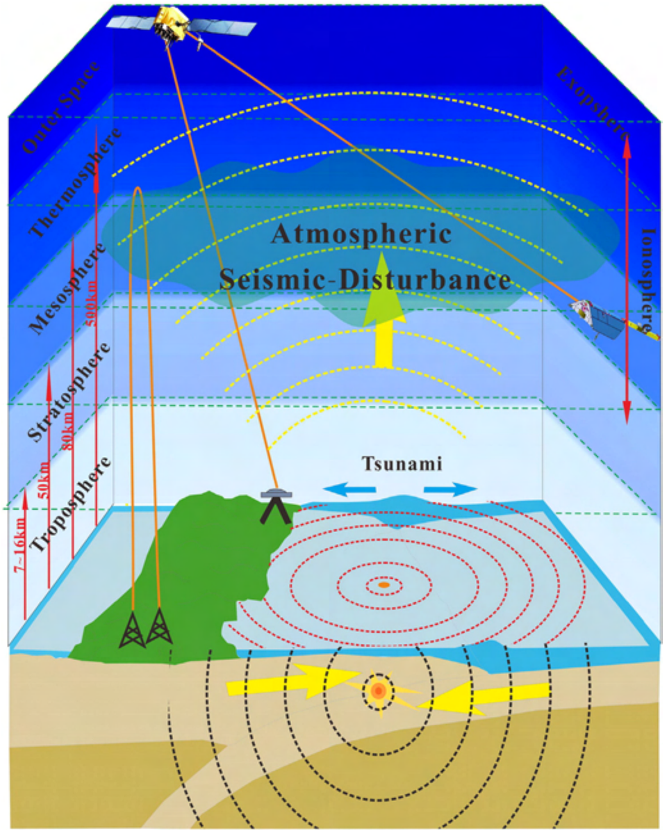

Fig. 3. Seismic–ionospheric disturbances from GNSS observations.

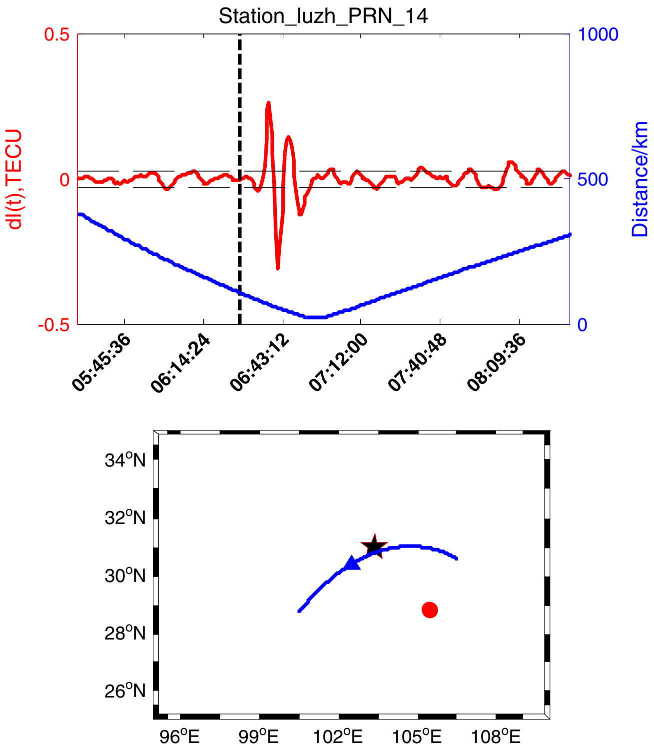

Fig. 4. TEC disturbances over LUZH station with PRN 14 on May 12, 2008. In the upper panel, the left vertical axis is the vertical TEC residual (dI(t),TECU) after 3–10 min filtering and the right axis is the distance between IPP and epicenter. The bottom panel shows the IPP tracks (arrow line), epicenter (star) and station (dot).

3. Atmospheric behaviors to recent strong earthquakes

3.1. 2008 Mw = 8.0 Wenchuan earthquake

The TEC variations are obtained from 28 continuous GPS sites of the CMONC. Fig. 4 shows the amplitude of the TEC disturbance following the 2008 Mw = 8.0 Wenchuan earthquake detected by the line-of-sight (LOS) between GPS station LUZH and satellite PRN 14. In the upper panel, the left vertical axis is the vertical TEC residual after 3–10 min filtering and the right axis is the horizontal distance between IPP and epicenter. The bottom panel shows the IPP tracks (arrow line), epicenter (star) and station (dot). Dramatic disturbance appears several minutes after the main shock. The disturbance is presented as an N-shaped pulse. Its amplitude decreases rapidly with the increase of the time and the distance of IPP's location and the epicenter.

The ionospheric TEC has the secular and regular changes, e.g., diurnal and seasonal scales, and abnormal variations caused by irregular events, such as geomagnetic storms, rocket launching, and possible solid-Earth events due to the lithosphere–ionosphere coupling. We have checked the ionospheric activity indices around the 2008 Mw = 8.0 Wenchuan earthquake on May 12, 2008, including the F10.7 cm solar radio flux, Auroral Electrojet (AE) and geomagnetic indices (Dst and Kp) and found relatively quiet days during this event. Therefore, the TEC disturbance at luzh station is mainly caused by the Wenchuan earthquake. In order to further confirm our results, 3 days of 28 continuous GPS station data from the Crustal Movement Observation Network of China (CMONC) are used from May 11–13, 2008. We filter the TEC time series dI(t) at 28 continuous GPS stations through removing the trend and regular changes with a window width of 3–10 min to obtain seismo-ionospheric disturbance characteristics (Jin et al., 2010; Kiryushkin and Afraimovich, 2007). Moreover, an accumulated mean TEC disturbance is calculated for all GPS stations. Significant seismo-ionospheric disturbances are found over GPS stations within about 500 km far from the epicenter during the main shock on May 12, 2008, while there are no apparent disturbances on the day before or after the main shock. Fig. 5 shows clear TEC disturbances during the May 12, 2008 Wenchuan earthquake with the main shock marked by the blue triangle (Afraimovich et al., 2010). Panel a. is the filtered TEC time series for satellite PRN22 at LUZH station on May 11, 12 and 13, 2008 with the black, red and gray lines, respectively, panel b. shows the response shape with the distance from the epicenter for satellites

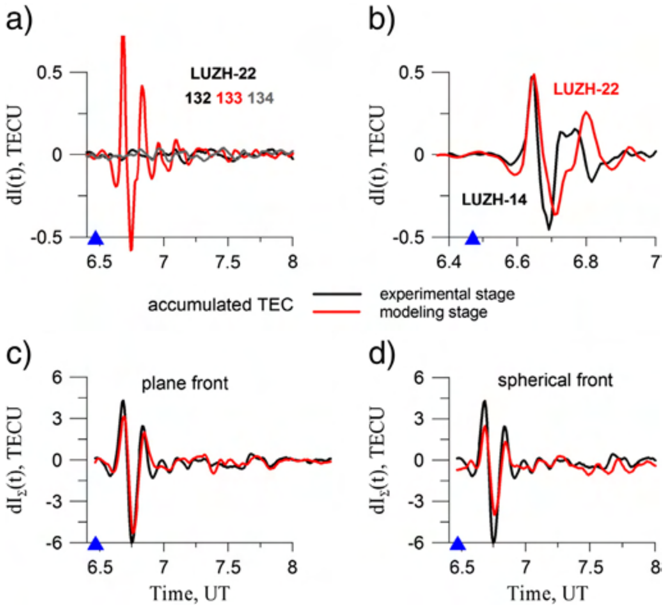

Fig. 5. TEC disturbances during the main shock of the May 12, 2008 Wenchuan earthquake marked by the blue triangle (Afraimovich et al., 2010). a) is the filtered TEC time series for satellite PRN22 at LUZH station on May 11, 12 and 13, 2008 with the black, red and gray lines, respectively, b) shows the response shape with the distance from the epicenter for satellites PRN22 and PRN14 at LUZH station, and c) and d) are the summarized TEC disturbance time series on the experimental stage (black line) and modeling stage (red line). (For interpretation of the references to color in this figure legend, the reader is referred to the web version of this article.)

PRN22 and PRN14 at LUZH station, and panel c. and panel d. are the summarized TEC disturbance time series on the experimental stage (black line) and modeling stage (red line). It clearly sees a significant seismo-ionospheric disturbance during the 2008 Wenchuan earthquake. Furthermore, a strong acoustic wave of N-shape shock is found with a plane waveform and a half-period of about 200 s propagating northeastward at an average speed of 600 m/s. The disturbance wavefront is nearly parallel with the rupture direction. The directional divergence of the seismic ionospheric disturbance may be the reason for the insufficient correspondence between the experiment and model based on the spherical wavefront approximation. More detailed information and results are referred to Afraimovich et al. (2010).

3.2. 2011 Mw = 9.0 Tohoku earthquake

The seismic ionospheric disturbances following the Tohoku earthquake are investigated using the detrended TEC series. Fig. 6 shows the tracks of satellite IPP distribution close to the epicenter (star). The detrended TEC time series are obtained by removing the linear items for every 10 min. The trend is mainly caused by IPP's motion and ionospheric rapid change. In quiet condition, the variation is smooth and can be considered as linear variation in 10 min. Here we do not run an average for the detrended TEC series as Tsugawa (*2011*), since the TEC time series derived from carrier phase observations have a high precision and are not affected by observation noise greatly. Furthermore, we can keep more high frequency signals in the detrended TEC time series and also avoid the disturbance amplitude attenuation due to the average process. Some recent studies comparing the unperturbed TEC (red line in Fig. 7) with the perturbed TEC (blue line in Fig. 7) have found an enhancement before the event or a hole (decreasing) just after and before the main shockwave (Heki, 2011; Kakinami et al., 2012; Heki and Enomoto, 2013). The doubt about the pre-seismic enhancement is that the post-seismic decrease will pull down the fit lines and the pre-seismic enhancement probably is a fake signal. Some recent works were trying to dynamically explain the hole formation as a consequence of the neutral-plasma coupling during the wave propagation. More difficult is the effort to support the hypothesis of the enhancement that involves electromagnetic behavior of the fault before the rupture.

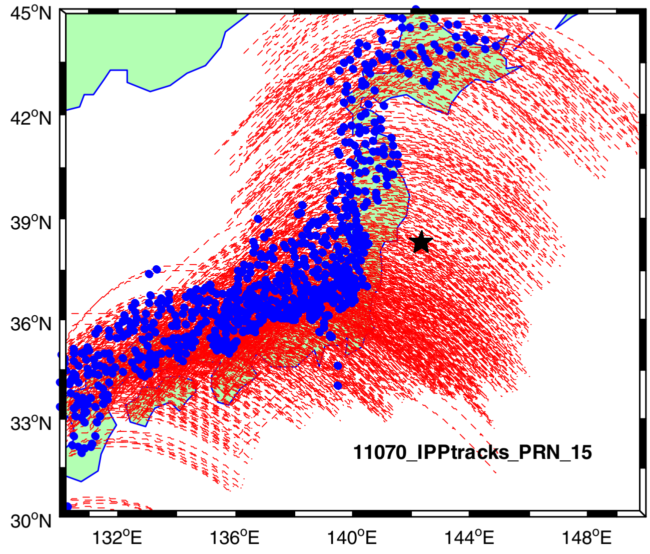

Fig. 6. The distribution of IPP tracks during the Tohoku earthquake (UTC 04:46–07:46) observed by GEONET. Each red line stands for GNSS stations and the star shows the epicenter. The blue dots mark the IPP location corresponding to the onset. (For interpretation of the references to color in this figure legend, the reader is referred to the web version of this article.)

Fig. 8 shows the distribution of whole VTEC anomaly time offsets corresponding to onset of the Tohoku earthquake occurred on March 11, 2011. Here we get rid of arcs whose peak anomalous values are less than 0.1 TECU to avoid the normal disturbance in GPS TEC observations, which are caused by measurement noise. Zero in horizontal axis is corresponding to the main shock time of the earthquake. We can see that lots of disturbances are found about 4 h before the main shock. This phenomenon may be the precursors of strong earthquake. Comparing to pre-seismic effects, post-seismic is more apparent. The first peak

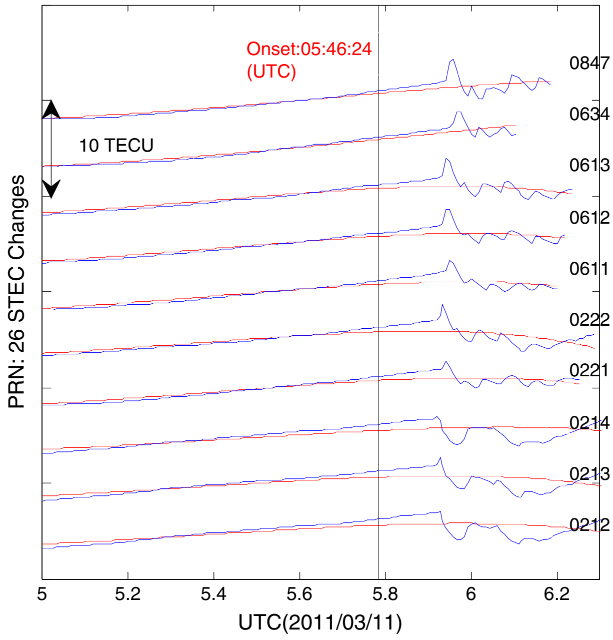

Fig. 7. TEC disturbances following the Tohoku earthquake on March 11, 2011. The red line shows the unperturbed TEC and blue line is the observed TEC disturbance. (For interpretation of the references to color in this figure legend, the reader is referred to the web version of this article.)

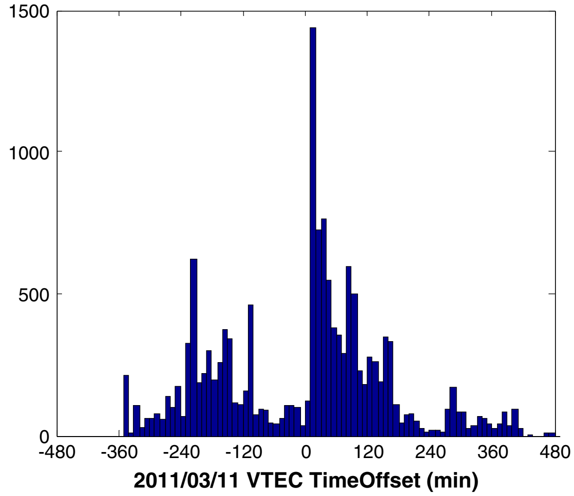

Fig. 8. Distribution of vertical TEC anomaly time offsets corresponding to onset of the Tohoku earthquake occurred on March 11, 2011. Here the arcs with less than 0.1 TECU maximum amplitude are not counted.

appears 10 min after the main shock. Disturbances are attenuating with the time, and sudden increase of anomalous arc occurs about 80 min and 150 min after onset. Fig. 8 also shows three types of disturbances after the strong earthquake happened on March 11, 2011. These three peaks should be related to the different types of atmospheric waves, such as acoustic wave in near-field, acoustic wave generated by Rayleigh wave propagation, tsunami-generated wave, and aftershock effect (Jin et al., 2014).

The ionospheric disturbance spreads out from the epicenter as a quasi-circular propagation pattern with the time, reproducing the seismic radiation diagram and the formation of Rayleigh wave (Rolland et al., 2011). Fig. 9 shows the TEC residual distribution following main-shock epoch in Japan every half hour. The residual amplitude is corresponding to −0.5 TECU or 0.5 TECU. The black star stands for the location of Tohoku earthquake's epicenter. In most areas, the disturbance amplitudes are 0.1–0.2 TECU. The disturbances with large amplitudes occurred above the Japan Sea, except the epicenter region. The large amplitudes are up to 1–2 TECU. The strong disturbances last nearly two hours from UTC 6:00 to 8:00. Above the East Sea, the relatively strong disturbances are found. At UTC 08:16, the TEC recovers to the state before the main shock as shown by the first and last subfigures in Fig. 9.

Fig. 10 shows the relationship between the average detrended TEC amplitudes and distances between the position of sub ionospheric pierce point (SIP, projection of IPP on the ground) and epicenter. The blue line is onset of the Tohoku earthquake in the Distance-UTC plane. The strongest disturbances mainly appear in the near field. The seismic ionospheric disturbance amplitudes decrease dramatically with the SIPs' location far away from the epicenter, especially in the near field (Jin et al., 2014). For the amplitude variation near the epicenter (0–500 km), three peaks are visible in the amplitude series. The disturbances related to the Rayleigh wave and acoustic wave spread out to 500 km away in about ten minutes, indicating that the disturbance effects induced by the first two waves are slight after UT 06:06, considering the time delay of the disturbance propagating from ground to the ionospheric height. So the two secondary peaks may be related to the two stronger aftershocks. For 500–1500 km, the average amplitudes are attenuated much more slowly.

Fig. 11 shows the relationship between time offset and IPP distance from the epicenter. We can see clearly quasi straight line stripes with several minutes of interval, and for each stripe, its color value decreases gradually in general expect for a sudden increasing that occurred about 40 min after the main shock epoch. These sudden increases have a relationship with the Mw = 8.0 after-shock in this region. The stripes' slopes, called disturbance velocities here, mainly ranging from 2000 m/s to 3200 m/s, 500 m/s to 1200 m/s and 120 m/s to 270 m/s are displayed in Fig. 11. The first and second propagation modes begin at about 10 min after main shock epoch, while the third propagation mode begins several minutes later. The source mechanism is the acoustic-gravity wave generated by the vertical displacement of the shock that reaches the ionosphere in 8–10 min (Occhipinti et al., 2013) and propagates until the first 1000 km (Liu et al., 2011), a pure acoustic wave coupled with the Rayleigh wave that propagates with a horizontal speed of 3.5 km/s and later a pure gravity wave coupled with the tsunami propagation that reaches the ionosphere in 40–50 min and visible in the ionosphere at the epicentral distance of around 500 km (Occhipinti et al., 2013).

Obvious disturbances in filtered TEC series with multi-frequencies are found with several minutes after the main shock. The multi-frequency disturbances from GPS ionospheric TEC can detect the acoustic wave and the Rayleigh wave (3–7 mHz) and tsunami-generated gravity wave (<3 mHz) (Matsumura et al., 2011; Occhipinti et al., 2013). Fig. 12 shows the variations of the mean value and the RMS (root mean square) of the filtered TEC series with the different band pass windows during UTC 5:00–9:00 in March, 2011 (Jin et al., 2014). The main shock and two aftershocks with Mw > 7 are marked by the beach balls. The mean seismic ionospheric disturbance with 1–3 mHz has larger amplitude than the one with 3–7 mHz. With the increase of the spreading time, the high frequency disturbance attenuates faster. In addition, a second ionospheric disturbance with 3–7 mHz in 300 km far from the epicenter appears several minutes after the first giant aftershock (Mw7.9) and reaches the maximum in 10 min, similar to the ionospheric anomaly variations of the main shock.

The ionospheric disturbances related to the Rayleigh wave, acoustic wave and tsunami-generated gravity wave are probably produced following giant earthquakes (Ducic et al., 2003; Artru et al., 2004; Occhipinti et al., 2013). The Rayleigh and acoustic wave propagate with the speed of about 2–3 km/s and around 1 km/s, respectively (Heki et al., 2006). From the in-situ ocean Bottom Pressure Records (BPR), two obvious disturbances are found in three ocean bottom pressure residual series (Jin et al., 2014). The first disturbance with a speed of 3071 m/s is related to the seismic Rayleigh wave, while the second one with a speed of 234 m/s is related to the tsunami propagation. From the TEC disturbance frequency, the tsunami-generated gravity wave is less than 3 mHz, while the Brünt–Vaïsalla frequency is in order of 3 mHz. Due to the time shifts corresponding to peaks of average 3–7 mHz TEC disturbances, the waves spread out from the near-filed to the far-filed with speeds of several kilometers per second, which are more consistent with the Rayleigh wave. In addition, it has been found that not only the main shock but also the giant aftershocks seismic ionospheric with acoustic mode could be detected by GPS measurement even though their intervals are no longer than one hour (see more details in Jin et al., 2014). Furthermore we investigate TEC disturbances following amount of aftershocks with Mw < 7, but no significant TEC disturbances are found.

4. Tsunami-generated gravity wave coupling

The detection of the tsunami signal in the ionosphere slowly follows observations of the seismic signature in the ionosphere related to the source displacement or to the propagation of Rayleigh waves. Indeed, the pure gravity wave generated by the tsunami in the overlying atmosphere/ionosphere creates a similar signature of the usually detected Traveling Ionospheric Disturbances (TID) (Artru et al., 2005). Therefore, the first undoubtful observation of the tsunami signal in the ionosphere followed the Great Sumatra event (Mw = 9.1, December 2004). The tsunami wave propagation in the Indian Ocean was broadly detected by ionospheric sounding with different techniques, mainly the TEC from GPS (DasGupta et al., 2006; Liu et al., 2006) and Altimeters (Occhipinti et al., 2006). The observations were clearly supported by

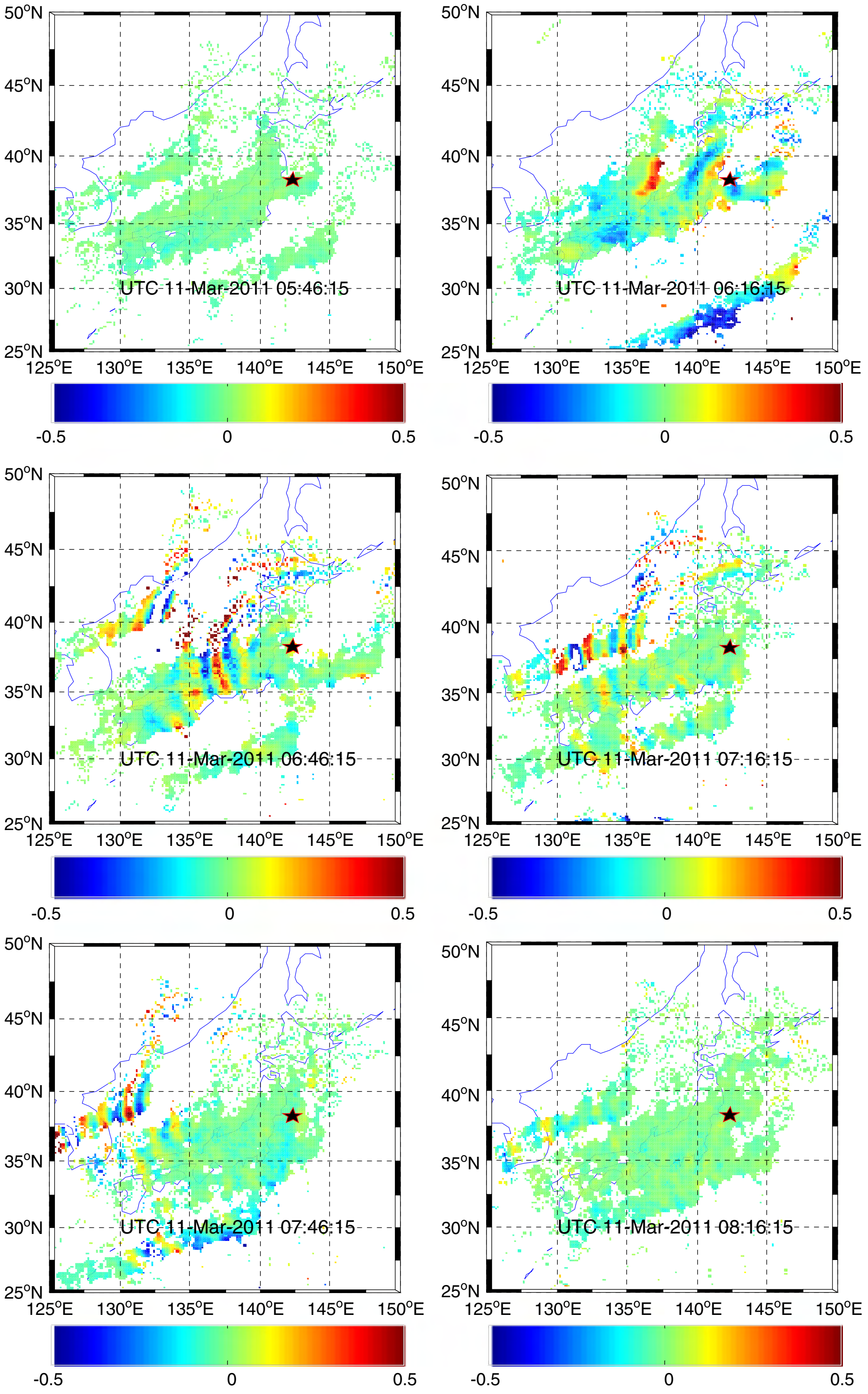

Fig. 9. TEC residual maps following main-shock epoch in Japan region every half hour. The residual amplitude is corresponding to −0.5 TECU or 0.5 TECU. The black star stands for the location of Tohoku earthquake's epicenter.

3-D numerical modeling (Occhipinti et al., 2006). In the following we resume the theoretical works of Occhipinti et al. (2006, 2008, 2013) on the coupling between the atmosphere–ionosphere and the tsunami. Then we emphasize the more recent tsunami detection by ionospheric sounding (Occhipinti et al., 2011).

The tsunami is an oceanic internal gravity wave (IGW) induced by the large volume displacement of ocean or lake water, which is a long period gravity wave with the frequency smaller than the atmospheric Brunt–Vaisalla frequency (Lognonné et al., 1998; Satake, 2002; Occhipinti et al., 2008). Based on the linear analysis, an internal gravity wave, coupled with the tsunami, is also generated in the overlying atmosphere (Hines, 1972; Occhipinti et al., 2006). To understand the tsunami–IGW propagation and mechanism of the tsunami–atmosphere coupling, a Bussinesq approximation is used (Spiegel and Veronis,

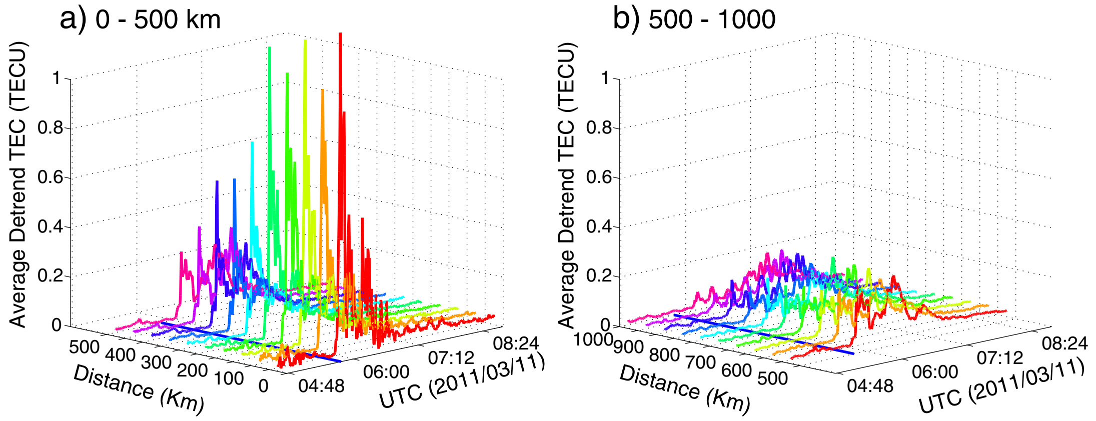

Fig. 10. Average amplitudes of the absolute detrended TEC variations with the distance to the epicenter during UTC 04:46–08:46 for 0–500 km (a) and 500–1000 km (b). (For interpretation of the references to color in this figure legend, the reader is referred to the web version of this article.)

1960). On the basis of the Navier–Stokes equation, Occhipinti et al. (2006, 2008) have developed a pseudo-spectral propagator $\frac{dV}{dz} = A \cdot V$ with the vector V and the matrix A as:

$$V = \begin{pmatrix} \tilde{u}_z^* \\ P^* \end{pmatrix} \tag{5}$$

$$A = \begin{pmatrix} -\frac{1}{\Omega}\left(k_x \frac{du_{x0}}{dz} + k_y \frac{du_{y0}}{dz}\right) & \frac{1}{2}\frac{d\ln\rho_0}{dz} - \frac{i\left(k_x^2 + k_y^2\right)}{\Omega} \\ i\left(\Omega + \frac{g}{\Omega}\frac{d\ln\rho_0}{dz}\right) & -\frac{1}{2}\frac{d\ln\rho_0}{dz} \end{pmatrix} \tag{6}$$

where $\tilde{u}_z^* = \sqrt{\rho_0}\tilde{u}_z$ and $P^* = \frac{\tilde{P}}{\sqrt{\rho_0}}$ are the normalized vertical velocity $\tilde{u}_z$ and pressure $\tilde{P}$ under the *omega-k* domain, respectively, $\Omega = \omega - u_{x0}k_x - u_{y0}k_y$ is the frequency induced by the wind (Sun et al., 2007; Nappo, 2012), ρ_0 is the unperturbed atmospheric density, u_{x0} and u_{y0} are the meridional and zonal background wind, respectively. Following Occhipinti et al. (2013), for a realistic atmosphere, the vertical *k*-number k_z and the frequency ω can be expressed as:

$$\begin{aligned} k_z &= \sqrt{{k_h}^2\left(\frac{N^2}{\omega^2} - 1\right) - \left(\frac{N^2}{2g}\right)^2} \\ \omega^2 &= \frac{{k_h}^2 N^2}{{k_z}^2 + {k_h}^2 + \left(\frac{N^2}{2g}\right)^2}. \end{aligned} \tag{7}$$

Therefore, the horizontal and vertical group velocity ${v_g}^h$ and ${v_g}^z$ can be estimated as:

$$\begin{aligned} {v_g}^h &= \frac{\partial\omega}{\partial k_h} = \frac{k_h N^2\left(D - {k_h}^2\right)}{\omega D^2} \\ {v_g}^z &= \frac{\partial\omega}{\partial k_z} = \frac{k_z {k_h}^2 N^2}{\omega D^2} \end{aligned} \tag{8}$$

where $D = {k_z}^2 + {k_h}^2 + \left(\frac{N^2}{2g}\right)^2$ is the denominator of the associated dispersion equation. Fig. 12 shows the vertical a. and horizontal b. IGW group velocities with the ocean depth with ocean–tsunamis–atmosphere coupling. The vertical group velocity is very important, while the horizontal group velocity is also useful to estimate the epicenter distance where the IGWs begin interacting with the ionosphere.

In addition, when IGWs reach and interact with the ionospheric plasma, it will result in a perturbation in the plasma density and velocity due to collisions between the ions and neutral molecules. Recently, several works have been performed and validated in detecting the tsunami by GNSS ionospheric TEC, e.g., tsunamis following the great 2004 Mw = 9.1 Sumatra earthquake, 2010 Chile earthquake and 2011 Mw = 9.0 Tohoku Earthquake (Rolland et al., 2010; Occhipinti et al., 2013; Galvan et al., 2012). Furthermore, numerical modeling of IGW reproduces the main features observed in the airglow images, which show interesting likenesses between the model and data, and explain the nature of the airglow observation and the role of the bathymetry in the ionospheric observation (Occhipinti et al., 2011). In the near future, a more complex three-dimensional (3-D) modeling on the tsunami–atmosphere–ionosphere coupling should be done with the viscosity and thermal conduction as already tested in a 1D case by Hickey et al. (2009).

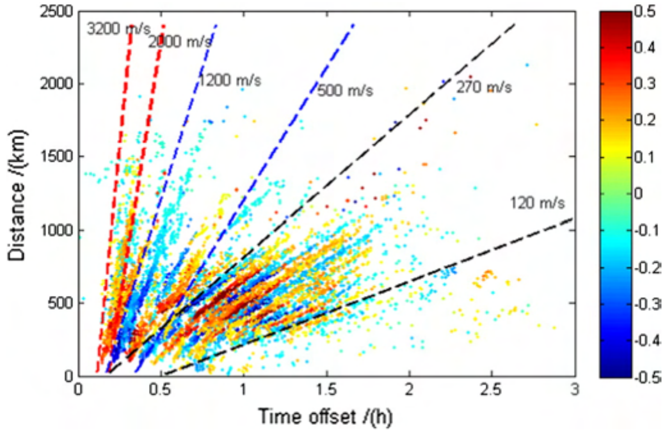

Fig. 11. Time offset referring to the epoch of main shock versus IPP distance from the epicenter. Origin of the axes stands for the main shock epoch and the epicenter location of Tohoku earthquake. Each dot is corresponding to the peak TEC residual of one TEC residual series. Here residual values of larger than 0.5 TECU are set as 0.5 and smaller than −0.5 TEC are set as −0.5 TECU.

5. Conclusion

In this paper, methods and progresses of GNSS ionospheric seismology are introduced and some case studies are presented. The seismo-ionospheric disturbances following the 2008 Mw = 8.0 Wenchuan

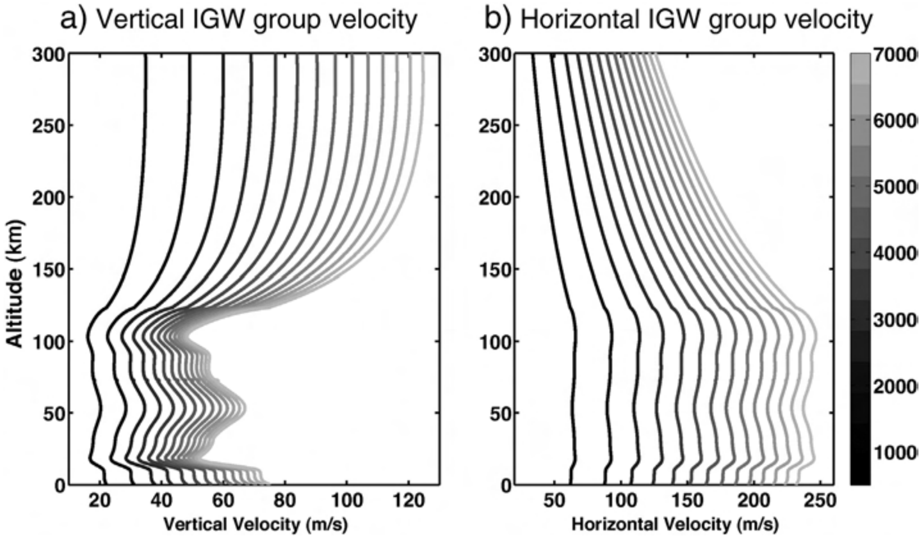

Fig. 12. The vertical (a) and horizontal (b) IGW group velocities with the ocean depth with ocean–tsunamis–atmosphere coupling.

earthquake and the 2011 Mw = 9.0 Tohoku earthquake are found by denser continuous GNSS observations. For the 2008 Mw = 8.0 Wenchuan earthquake, smaller disturbance amplitudes are detected and its maximum value is about 0.5 TECU, while its duration is shorter and disturbance areas are smaller. Furthermore, the co-seismic ionospheric disturbances are mainly driven by the lithosphere–ionosphere coupled air waves from the vertical motion of seismic waves. For March 11, 2011 Mw = 9.0 Japan earthquake, significant seismo-ionospheric disturbances are found with up to 2 TECU. The most propagation mode is ranging from 2000 m/s to 3200 m/s, 500 m/s to 1200 m/s and 120 m/s to 270 m/s. The seismo-ionospheric effects are related to not only the main shock, but also the two strongest aftershocks. Disturbance amplitude deceases rapidly in 0–500 km far from the epicenter. The ionospheric perturbations related to tsunami and/or Rayleigh wave propagation are detectable at teleseismic distances. The ionospheric effects following the Tohoku earthquake are attenuated with the increase of the time and distance between the IPP and the epicenter, especially in the near field. In general, the post-seismic ionospheric disturbance spreads out with three patterns, which are related to the source displacement, to the Rayleigh wave, and the tsunami. As more and more GNSS continuous operating stations and Multi GNSS constellations, it is possible to estimate the source extent with seismic–ionospheric effect based on the theory of solid earth/ocean atmosphere coupling. The basic parameters of earthquake, such as epicenter location and main shock time, could be estimated rapidly with the seismic–ionospheric propagation if there are enough GNSS measurements around the epicenter. With this work we wish to motivate future works in GNSS ionospheric seismology to estimate the source extent and the magnitude in order to support the classic techniques for earthquake and tsunami warning system.

Acknowledgment

This research is supported by the Main Direction Project of Chinese Academy of Sciences (Grant No. KJCX2-EW-T03), National Natural Science Foundation of China (NSFC) Project (Grant Nos. 11173050 and 11373059), Shanghai Science and Technology Commission Project (Grant No. 12DZ2273300) and Key Laboratory of Plenatary Sciences, Chinese Academy of Sciences. G.O. is supported by the Programme National de Télédétection Spatiale (PNTS) (Grant No. PNTS-2014-07) and by the CNES grant SI-EuroTOMO and IONOGLOW. This is also the IPGP contribution 3634.

References

Afraimovich, E.L., Ding, F., Kiryushkin, V., Astafyeva, E., Jin, S.G., Sankov, V., 2010. TEC response to the 2008 Wenchuan earthquake in comparison with other strong earthquakes. Int. J. Remote Sens. 31 (13), 3601–3613.

Afraimovich, E.L., Ishina, A., Tinin, M., Yasyukevich, Y., Jin, S.G., 2011. First evidence of anisotropy of GPS phase slips caused by the mid-latitude field-aligned ionospheric irregularities. Adv. Space Res. 47 (10), 1674–1680.

Artru, J., Farges, T., Lognonné, P., 2004. Acoustic waves generated from seismic surface waves: propagation properties determined from Doppler sounding observations and normal-mode modelling. Geophys. J. Int. 158 (3), 1067–1077.

Artru, J., Ducic, V., Kanamori, H., et al., 2005. Ionospheric detection of gravity waves induced by tsunamis. Geophys. J. Int. 160 (3), 840–848.

Astafyeva, E., Lognonne, P., Rolland, L., 2011. First ionospheric images of the seismic fault slip on the example of the Tohoku-oki earthquake. Geophys. Res. Lett. 38 (22), L22104. http://dx.doi.org/10.1029/2011GL049623.

Astafyeva, E., Rolland, L., Lognonne, P., Khelfi, K., Yahagi, T., 2013. Parameters of seismic source as deduced from 1 Hz ionospheric GPS data: case study of the 2011 Tohoku-oki event. J. Geophys. Res. Space Phys. 118 (9), 5942–5950.

Blewitt, G., 1990. An automatic editing algorithm for GPS data. Geophys. Res. Lett. 17 (3), 199–202.

Brunini, C., Azpilicueta, F.J., 2009. Accuracy assessment of the GPS-based slant total electron content. J. Geodesy 83 (8), 773–785.

Cai, C., Liu, Z., Xia, P., Dai, W., 2013. Cycle slip detection and repair for undifferenced GPS observations under high ionospheric activity. GPS Solutions 17 (2), 247–260.

Calais, E., Minster, J.B., 1995. GPS detection of ionospheric perturbations following the January 17, 1994, Northridge earthquake. Geophys. Res. Lett. 22 (9), 1045–1048.

Cambiotti, G., Bordoni, A., Sabadini, R., Colli, L., 2011. GRACE gravity data help constraining seismic models of the 2004 Sumatran earthquake. J. Geophys. Res. Solid Earth 116 (B10), B10403. http://dx.doi.org/10.1029/2010JB007848.

Coisson, P., Occhipinti, G., Lognonné, P., Molinie, J.P., Rolland, L., 2011. Tsunami signature in the ionosphere: a simulation of OTH radar observations. Radio Sci. 46, RS0D20. http://dx.doi.org/10.1029/2010RS004603.

DasGupta, A., Das, A., Hui, D., KBandyopadhyay, K., Sivaraman, M.R., 2006. Ionospheric perturbations observed by the GPS following the December 26th, 2004 Sumatra–Andaman earthquake. Earth Planets Space 58 (2), 167–172.

Davies, K., Baker, D.M., 1965. Ionospheric effects observed around the time of the Alaskan earthquake of March 28, 1964. J. Geophys. Res. 70 (9), 2251–2253.

der Hilst, B.H., 2008. A geological and geophysical context for the Wenchuan earthquake of 12 May 2008, Sichuan, People's Republic of China. GSA Today 18 (7), 4–11.

Ducic, V., Artru, J., Lognonné, P., 2003. Ionospheric remote sensing of the Denali Earthquake Rayleigh surface waves. Geophys. Res. Lett. 30 (18), 1951. http://dx.doi.org/10.1029/2003GL017812.

Galvan, D.A., Komjathy, A., Hickey, M.P., et al., 2012. Ionospheric signatures of Tohoku-Oki tsunami of March 11, 2011: model comparisons near the epicenter. Radio Sci. 47 (4), RS4003. http://dx.doi.org/10.1029/2012RS005023.

Heki, K., 2011. Ionospheric electron enhancement preceding the 2011 Tohoku-Oki earthquake. Geophys. Res. Lett. 38 (17), L17312. http://dx.doi.org/10.1029/2011GL047908.

Heki, K., Enomoto, Y., 2013. Preseismic ionospheric electron enhancements revisited. J. Geophys. Res. Space Phys. 118 (10), 6618–6626.

Heki, K., Ping, J., 2005. Directivity and apparent velocity of the coseismic ionospheric disturbances observed with a dense GPS array. Earth Planet. Sci. Lett. 236 (3), 845–855.

Heki, K., Otsuka, Y., Choosakul, N., Hemmakorn, N., Komolmis, T., Maruyama, T., 2006. Detection of ruptures of Andaman fault segments in the 2004 great Sumatra earthquake with coseismic ionospheric disturbances. J. Geophys. Res. Solid Earth 111 (B9), B09313. http://dx.doi.org/10.1029/2005JB004202.

Hickey, M.P., Schubert, G., Walterscheid, R.L., 2009. Propagation of tsunami-driven gravity waves into the thermosphere and ionosphere. J. Geophys. Res. Space Phys. 114 (A8), A08304.

Hines, C.O., 1972. Gravity waves in the atmosphere. Nature 239, 73–78.

Jakowski, N., Hoque, M.M., Mayer, C., 2011. A new global TEC model for estimating transionospheric radio wave propagation errors. J. Geodesy 85 (12), 965–974.

Jin, S.G., Wang, J., Zhang, H., Zhu, W., 2004. Real-time monitoring and prediction of the total ionospheric electron content by means of GPS observations. Chin. Astron. Astrophys. 28 (3), 331–337.

Jin, S.G., Li, Z.C., Cho, J.H., 2008a. Integrated water vapor field and multi-scale variations over China from GPS measurements. J. Appl. Meteorol. Climatol. 47 (11), 3008–3015.

Jin, S.G., Luo, O.F., Park, P.H., 2008b. GPS observations of the ionospheric F2-layer behavior during the 20th November 2003 geomagnetic storm over South Korea. J. Geodesy 82 (12), 883–892. http://dx.doi.org/10.1007/s00190-008-0217-x.

Jin, S.G., Zhu, W., Afraimovich, E., 2010. Co-seismic ionospheric and deformation signals on the 2008 magnitude 8.0 Wenchuan Earthquake from GPS observations. Int. J. Remote Sens. 31 (13), 3535–3543.

Jin, S.G., Han, L., Cho, J., 2011. Lower atmospheric anomalies following the 2008 Wenchuan Earthquake observed by GPS measurements. J. Atmos. Sol. Terr. Phys. 73 (7), 810–814.

Jin, R., Jin, S.G., Feng, G.P., 2012. M_DCB: Matlab code for estimating GNSS satellite and receiver differential code biases. GPS Solutions 16 (4), 541–548.

Jin, S.G., van Dam, T., Wdowinski, S., 2013. Observing and understanding the Earth system variations from space geodesy. J. Geodyn. 72, 1–10. http://dx.doi.org/10.1016/j.jog.2013.08.001.

Jin, S.G., Jin, R., Li, J.H., 2014. Pattern and evolution of seismo-ionospheric disturbances following the 2011 Tohoku earthquakes from GPS observations. J. Geophys. Res. Space Phys. 119 (9), 7914–7927.

Kakinami, Y., Kamogawa, M., Tanioka, Y., Watanabe, S., Gusman, A.R., Liu, J.-Y., Watanabe, Y., Mogi, T., 2012. Tsunamigenic ionospheric hole. Geophys. Res. Lett. 39 (13), L00G27. http://dx.doi.org/10.1029/2011GL050159.

Kamogawa, M., 2006. Preseismic lithosphere-atmosphere-ionosphere coupling. EOS Trans. Am. Geophys. Union 87 (40), 417–424.

Kamogawa, M., Kakinami, Y., 2013. Is an ionospheric electron enhancement preceding the 2011 Tohoku-Oki earthquake a precursor? J. Geophys. Res. Space Phys. 118 (4), 1751–1754.

Kiryushkin, V.V., Afraimovich, E.L., 2007. Determining the parameters of ionospheric perturbation caused by earthquakes using the quasi-optimum algorithm of spatio-temporal processing of TEC measurements. Earth Planets Space 59 (4), 267–278.

Leonard, R.S., Barnes, R.A., 1965. Observation of ionospheric disturbances following the Alaska earthquake. J. Geophys. Res. 70 (5), 1250–1253.

Liu, J.-Y., Chuo, Y.J., Shan, S.J., Tsai, Y.B., Chen, Y.I., Pulinets, S.A., Yu, S.B., 2004. Pre-earthquake ionospheric anomalies registered by continuous GPS TEC measurements. Ann. Geophys. 22 (5), 1585–1593.

Liu, J.-Y., Chen, Y.I., Chuo, Y.J., Chen, C., 2006. A statistical investigation of preearthquake ionospheric anomaly. J. Geophys. Res. Space Phys. 111 (A5), A05304. http://dx.doi.org/10.1029/2005JA011333.

Liu, J.-Y., Chen, C.-H., Lin, C.-H., Tsai, H.-F., Chen, C.-H., Kamogawa, M., 2011. Ionospheric disturbances triggered by the 11 March 2011 M9. 0 Tohoku earthquake. J. Geophys. Res. Space Phys. 116 (A6), A06319. http://dx.doi.org/10.1029/2011JA016761 (1978–2012).

Lognonné, P., Clévédé, E., Kanamori, H., 1998. Computation of seismograms and atmospheric oscillations by normal-mode summation for a spherical earth model with realistic atmosphere. Geophys. J. Int. 135 (2), 388–406.

Matsumura, M., Saito, A., Iyemori, T., Shinagawa, H., Tsugawa, T., Otsuka, Y., Nishioka, M., Chen, C.H., 2011. Numerical simulations of atmospheric waves excited by the 2011 off the Pacific coast of Tohoku Earthquake. Earth Planets Space 63 (7), 885–889.

Najita, K., Yuen, P.C., 1979. Long-period oceanic rayleigh wave group velocity dispersion curve from HF Doppler sounding of the ionosphere. J. Geophys. Res. Space Phys. 84 (A4), 1253–1260.

Nappo, C.J., 2012. An introduction to atmospheric gravity waves. vol. 102. Academic Press.

Occhipinti, G., Lognonné, P., Kherani, E.A., Hebert, H., 2006. Three-dimensional waveform modeling of ionospheric signature induced by the 2004 Sumatra tsunami. Geophys. Res. Lett. 33 (20), L20104. http://dx.doi.org/10.1029/2006GL026865.

Occhipinti, G., Kherani, E.A., Lognonné, P., 2008. Geomagnetic dependence of ionospheric disturbances induced by tsunamigenic internal gravity waves. Geophys. J. Int. 173 (3), 753–765.

Occhipinti, G., Dorey, P., Farges, T., Lognonne, P., 2010. Nostradamus: the radar that wanted to be a seismometer. Geophys. Res. Lett. 37, L18104. http://dx.doi.org/10.1029/2010GL044009.

Occhipinti, G., Coisson, P., Makela, J.J., Allgeyer, S., Kherani, A., Hebert, H., Lognonné, P., 2011. Three-dimensional numerical modeling of tsunami-related internal gravity waves in the Hawaiian atmosphere. Earth Planets Space 63 (7), 847–851.

Occhipinti, Giovanni, Rolland, Lucie, Lognonné, Philippe, Watada, Shingo, 2013. From Sumatra 2004 to Tohoku-Oki 2011: the systematic GPS detection of the ionospheric signature induced by tsunamigenic earthquakes. J. Geophys. Res. Space Phys. 118 (6), 3626–3636.

Perevalova, N.P., Sankov, V.A., Astafyeva, E.I., Zhupityaeva, A.S., 2014. Threshold magnitude for ionospheric TEC response to earthquakes. J. Atmos. Sol. Terr. Phys. 108, 77–90.

Pulinets, S., Boyarchuk, K., 2004. Ionospheric Precursors of Earthquakes. Springer Science & Business Media.

Pulinets, S., Ouzounov, D., 2011. Lithosphere–atmosphere–ionosphere coupling (LAIC) model—an unified concept for earthquake precursors validation. J. Asia Earth Sci. 41 (4), 371–382.

Rolland, L., Occhipinti, G., Lognonné, P., Loevenbruck, A., 2010. The 29 September 2009 Samoan tsunami in the ionosphere detected offshore Hawaii. Geophys. Res. Lett. 37, L17191.

Rolland, L.M., Lognonné, P., Astafyeva, E., Kherani, E.A., Kobayashi, N., Mann, M., Munekane, H., 2011. The resonant response of the ionosphere imaged after the 2011 off the Pacific coast of Tohoku Earthquake. Earth Planets Space 63 (7), 853–857.

Row, R.V., 1966. Evidence of long-period acoustic-gravity waves launched into the F region by the Alaskan earthquake of March 28, 1964. J. Geophys. Res. 71 (1), 343–345.

Row, R.V., 1967. Acoustic-gravity waves in the upper atmosphere due to a nuclear detonation and an earthquake. J. Geophys. Res. 72 (5), 1599–1610.

Satake, K., 2002. Tsunamis. In: Lee, W.H.K., Kanamori, H., Jenning, P.C., Kisslinger, C. (Eds.), International Geophysics Series 81A. Academic press.

Schaer, S., 1999. Mapping and predicting the Earth's ionosphere using the Global Positioning System. Geod. Geophys. Arb. Schweiz. 59 (59).

Schreiner, William S., Sokolovskiy, Sergey V., Rocken, Christian, Hunt, Douglas C., 1999. Analysis and validation of GPS/MET radio occultation data in the ionosphere. Radio Sci. 34 (4), 949–966.

Shinagawa, H., Tsugawa, T., Matsumura, M., Iyemori, T., Saito, A., Maruyama, T., Jin, H., Nishioka, M., Otsuka, Y., 2013. Two-dimensional simulation of ionospheric variations in the vicinity of the epicenter of the Tohoku-oki earthquake on 11 March 2011. Geophys. Res. Lett. 40 (19), 5009–5013.

Spiegel, E.A., Veronis, G., 1960. On the Boussinesq approximation for a compressible fluid. Astrophys. J. 131, 442.

Sun, L., Wan, W., Ding, F., Mao, T., 2007. Gravity wave propagation in the realistic atmosphere based on a three-dimensional transfer function model. Ann. Geophys. 25 (9), 1979–1986.

Tanaka, T., Ichinose, T., Okuzawa, T., Shibata, T., Sato, Y., Nagasawa, C., Ogawa, T., 1984. HF-Doppler observations of acoustic waves excited by the Urakawa–Oki earthquake on 21 March 1982. J. Atmos. Terr. Phys. 46 (3), 233–245.

Tsugawa, T., Saito, A., Otsuka, Y., Nishioka, M., Maruyama, T., Kato, H., Nagatsuma, T., Murata, K.T., 2011. Ionospheric disturbances detected by GPS total electron content observation after the 2011 off the Pacific coast of Tohoku Earthquake. Earth Planets Space 63 (7), 875–879.

Utada, H., Shimizu, H., 2014. Comment on "Preseismic ionospheric electron enhancements revisited" by K. Heki and Y. Enomoto. J. Geophys. Res. Space Phys. 119 (7), 6011–6015.

Wickert, J., Reigber, C., Beyerle, G., König, R., Marquardt, C., Schmidt, T., Grunwaldt, L., et al., 2001. Atmosphere sounding by GPS radio occultation: First results from CHAMP. Geophys. Res. Lett. 28 (17), 3263–3266.

Wu, Y., Jin, S.G., Wang, Z., Liu, J., 2010. Cycle slip detection using multi-frequency GPS carrier phase observations: a simulation study. Adv. Space Res. 46 (2), 144–149. http://dx.doi.org/10.1016/j.asr.2009.11.007.